

Colliding Alfvénic wave packets in MHD, Hall and kinetic simulations

O. Pezzi^{1†}, T.N. Parashar², S. Servidio¹, F. Valentini¹, C.L. Vásconez³, Y. Yang², F. Malara¹, W.H. Matthaeus² and P. Veltri¹

¹Dipartimento di Fisica, Università della Calabria, 87036 Rende (CS), Italy.

²Department of Physics and Astronomy, University of Delaware, DE 19716, USA.

³Departamento de Física, Escuela Politécnica Nacional, Quito, Ecuador.

(Received ?; revised ?; accepted ?. - To be entered by editorial office)

The analysis of the Parker–Moffatt problem, recently revisited in Pezzi *et al.* (2016), is here extended by including the Hall magnetohydrodynamics and two hybrid kinetic Vlasov-Maxwell numerical models. The presence of dispersive and kinetic features is studied in detail and a comparison between the two kinetic codes is also reported. Focus on the presence of non-Maxwellian signatures shows that - during the collision - regions characterized by strong temperature anisotropy are recovered and the proton distribution function displays a beam along the direction of the magnetic field, similar to some recent observations of the solar wind.

PACS codes: Authors should not enter PACS codes directly on the manuscript, as these must be chosen during the online submission process and will then be added during the typesetting process (see <http://www.aip.org/pacs/> for the full list of PACS codes)

1. Introduction

The interaction of two oppositely propagating Alfvénic wave packets has been studied for more than half a century. This interaction has been proposed as an elementary step in the analysis of magnetohydrodynamics (MHD) turbulence (Elsässer 1950; Iroshnikov 1964; Kraichnan 1965; Dobrowolny *et al.* 1980a,b; Velli *et al.* 1989; Sridhar & Goldreich 1994; Goldreich & Sridhar 1995; Ng & Bhattacharjee 1996; Matthaeus *et al.* 1999; Galtier *et al.* 2000; Verdini *et al.* 2009; Howes & Nielson 2013; Nielson *et al.* 2013). Indeed, in the framework of ideal incompressible magnetohydrodynamics (MHD), large amplitude perturbations in which the magnetic \mathbf{b} and bulk velocity \mathbf{u} fluctuations are either perfectly correlated, or perfectly anti-correlated, are solutions of the governing equations. To induce nonlinear couplings among the fluctuations, and therefore to excite turbulence, it is necessary to simultaneously consider magnetic fluctuations \mathbf{b} and velocity fluctuations \mathbf{u} that have an arbitrary sense of correlation. This may be accomplished by superposing the two senses of correlation, in Alfvén units, $\mathbf{u} = +\mathbf{b}$ and $\mathbf{u} = -\mathbf{b}$.

Based on these considerations, Moffatt (1978) and Parker (1979) analyzed the collision of large-amplitude Alfvén wave packets in the framework of the incompressible MHD, observing that their interaction is limited to the time interval in which they overlap. During this temporal window wave packets can transfer energy and modify their spatial structure; however, after the collision, packets return to undisturbed propagation without further interactions. The Parker–Moffatt problem has been recently revisited in (Pezzi *et al.*

† Email address for correspondence: oreste.pezzi@fis.unical.it

2016) (hereafter, Paper I) with the motivation to extend its description to the realm of the kinetic plasmas. In fact, the scenario described by Parker & Moffatt is potentially applicable to astrophysical plasmas such as solar wind (Belcher & Davis 1971; Bruno *et al.* 1985; Verdini *et al.* 2009) or solar corona (Matthaeus *et al.* 1999; Tomczyk *et al.* 2007), where Alfvénic perturbations represent one of the main components of fluctuations. However, since such systems often exhibit compressive activity as well as dispersion and kinetic signatures (Alexandrova *et al.* 2008; Bruno & Carbone 2013; Sahraoui *et al.* 2007; Gary *et al.* 2010; Marsch 2006; Valentini *et al.* 2011; Servidio *et al.* 2012; Valentini *et al.* 2014; Servidio *et al.* 2015; He *et al.* 2015; Roberts *et al.* 2016; Lion *et al.* 2016; Perrone *et al.* 2016), it is of considerable interest to include these features in the analysis of the *Parker & Moffatt* problem.

In particular, in Paper I, it has been found that during the wave packets interaction, as prescribed by *Parker & Moffatt*, nonlinear coupling processes cause the magnetic energy spectra to evolve towards isotropy, while energy transfers towards smaller spatial scales. Moreover, the new ingredients introduced with the kinetic simulation (Hall and kinetic effects) play a significant role and several features of the evolution in the Vlasov case differ with respect to the MHD evolution. Here we extend that study to discern the role of dispersive and genuinely kinetic effects, supplementing the previously considered MHD and Vlasov simulations, by introducing also an Hall MHD simulation. Moreover, we also examine this basic problem by means of a hybrid Particle-in-Cell simulation (HPIC), which allows comparison of two different numerical approaches (HVM and HPIC), which refer to the same physical model. We may anticipate that, in the HPIC case, the system dynamics at small scales is affected by the presence of particles thermal noise and only the features related to large spatial scales are properly recovered during the evolution of the two wave packets. Based on this consideration, we employ mainly the HVM simulation to highlight the presence of kinetic effects during the wave packets interaction. In particular, during the collision of the wave packets, the proton velocity distribution function (VDF) exhibits a beam along the background magnetic field direction, similar to some solar wind observations (He *et al.* 2015). We note that the present paper compares results from four different models in the context of a single physical problem, and is therefore also a contribution in the spirit of the “Turbulence Dissipation Challenge” that has been recently discussed in the space plasma community Parashar *et al.* (2015b).

The paper is organized as follows: in Sec. 2 the theoretical model and the numerical codes are presented. In Sec. 3, we compare the several simulations by focusing on the description of some fluid-like diagnostics. Sec. 4, examines kinetic signatures in the HVM simulation. Finally we conclude in Sec. 5 by summarizing our results.

2. Theoretical models and numerical approaches

As discussed above, here we approach the problem concerning the interaction of two Alfvénic wave packets by means of fluid and hybrid numerical simulations. For problems such as this, the system dimensionality is fundamental: in fact, a proper description should consider a three-dimensional physical space (i.e. three-dimensional wave vectors), where both parallel and perpendicular cascades are taken into account (Howes 2015; Parashar *et al.* 2015a, 2016). However, dynamical range of the spatial scales (wave numbers) represented in the model is equally important to capture nonlinear couplings during the wave packet interaction. Furthermore, performing a kinetic HVM simulation which contemporaneously includes a full $3D-3V$ phase space and while also retaining a good spatial resolution is too demanding for the present High Performance Computing capability. Given that numerous runs are required to complete a study such as the present

one, a fully 3D approach would be prohibitive. Therefore we adopt a 2.5D physical space, where vectorial fields are three-dimensional but their variations depend only on two spatial coordinates (x and y). It is worth noting that 2.5D captures the qualitative nature of many processes very well even though there might be some quantitative differences for some processes (Karimabadi *et al.* 2013; Wan *et al.* 2015; Li *et al.* 2016).

The fluid models here considered are MHD and Hall MHD, whose dimensionless equations are:

$$\partial_t \rho + \nabla \cdot (\rho \mathbf{u}) = 0 \quad (2.1)$$

$$\partial_t \mathbf{u} + (\mathbf{u} \cdot \nabla) \mathbf{u} = -\frac{\tilde{\beta}}{2\rho} \nabla(\rho T) + \frac{1}{\rho} [(\nabla \times \mathbf{B}) \times \mathbf{B}] \quad (2.2)$$

$$\partial_t \mathbf{B} = \nabla \times \left[\mathbf{u} \times \mathbf{B} - \frac{\tilde{\epsilon}}{\rho} (\nabla \times \mathbf{B}) \times \mathbf{B} \right] \quad (2.3)$$

$$\partial_t T + (\mathbf{u} \cdot \nabla) T + (\gamma - 1) T (\nabla \cdot \mathbf{u}) = 0 \quad (2.4)$$

In Eqs. (2.1)–(2.4) spatial coordinates $\mathbf{x} = (x, y)$ and time t are respectively normalized to \tilde{L} and $\tilde{t}_A = \tilde{L}/\tilde{c}_A$. The magnetic field $\mathbf{B} = \mathbf{B}_0 + \mathbf{b}$ is scaled to the typical magnetic field \tilde{B} , while mass density ρ , fluid velocity \mathbf{u} , temperature T and pressure $p = \rho T$ are scaled to typical values $\tilde{\rho}$, $\tilde{c}_A = \tilde{B}/(4\pi\tilde{\rho})^{1/2}$, \tilde{T} and $\tilde{p} = 2\kappa_B \tilde{\rho} \tilde{T}/m_p$ (being κ_B the Boltzmann constant and m_p the proton mass), respectively. Moreover, $\tilde{\beta} = \tilde{p}/(\tilde{B}^2/8\pi)$ is a typical value for the kinetic to magnetic pressure ratio; $\gamma = 5/3$ is the adiabatic index and $\tilde{\epsilon} = \tilde{d}_p/\tilde{L}$ (being $\tilde{d}_p = \tilde{c}_A/\tilde{\Omega}_{cp}$ the proton skin depth) is the Hall parameter, which is set to zero in the pure MHD case. Details about the numerical algorithm can be found in Vázquez *et al.* (2015); Pucci *et al.* (2016).

On the other hand, hybrid Vlasov-Maxwell simulations have been performed by using two different numerical codes: an Eulerian hybrid Vlasov-Maxwell code (HVM) (Valentini *et al.* 2007) and a hybrid Particle-in-cell (HPIC) code (Parashar *et al.* 2009). For both cases protons are described by a kinetic equation, while electrons are a Maxwellian, isothermal fluid. In the Vlasov model, an Eulerian representation of the Vlasov equation for protons is numerically integrated. In PIC method, the distribution function is Monte-Carlo discretized and the Newton-Lorentz equations are updated for the “macro-particles”. Electromagnetic fields, charge density and current density are computed on a grid (Birdsall & Langdon 2004; Dawson 1983).

Dimensionless HVM equations are:

$$\partial_t f + \mathbf{v} \cdot \nabla f + \frac{1}{\tilde{\epsilon}} (\mathbf{E} + \mathbf{v} \times \mathbf{B}) \cdot \nabla_{\mathbf{v}} f = 0 \quad (2.5)$$

$$\begin{aligned} \mathbf{E} - \frac{m_e \tilde{\epsilon}^2}{m_p} \Delta \mathbf{E} = & -\mathbf{u}_{\mathbf{e}} \times \mathbf{B} - \frac{\tilde{\epsilon} \tilde{\beta}}{2n} \left(\nabla P_e - \frac{m_e}{m_p} \nabla \cdot \Pi \right) + \\ & + \frac{m_e}{m_p} \left[\mathbf{u} \times \mathbf{B} + \frac{\tilde{\epsilon}}{n} \nabla \cdot (n(\mathbf{u}\mathbf{u} - \mathbf{u}_{\mathbf{e}}\mathbf{u}_{\mathbf{e}})) \right] \end{aligned} \quad (2.6)$$

$$\frac{\partial \mathbf{B}}{\partial t} = -\nabla \times \mathbf{E} \quad ; \quad \nabla \times \mathbf{B} = \mathbf{j} \quad (2.7)$$

where $f = f(\mathbf{x}, \mathbf{v}, t)$ is the proton distribution function. In Eqs. (2.5)–(2.7), velocities \mathbf{v} are scaled to the Alfvén speed \tilde{c}_A , while the proton number density $n = \int f d^3v$, the proton bulk velocity $\mathbf{u} = n^{-1} \int \mathbf{v} f d^3v$ and the proton pressure tensor $\Pi_{ij} = n^{-1} \int (v_i - u_i)(v_j - u_j) f d^3v$, obtained as moments of the distribution function, are normalized to $\tilde{n} = \tilde{\rho}/m_p$, \tilde{c}_A and \tilde{p} , respectively. The electric field \mathbf{E} , the current density $\mathbf{j} = \nabla \times \mathbf{B}$ and the electron pressure P_e are scaled to $\tilde{E} = (\tilde{c}_A \tilde{B})/c$, $\tilde{j} = c \tilde{B}/(4\pi \tilde{L})$ and \tilde{p} , respectively. Electron inertia effects have been considered in Ohm’s law to prevent numerical instabilities (being $m_e/m_p = 0.01$, where m_e is the electron mass), while no external resistivity η is introduced. A detailed description of the HVM algorithm can be found in

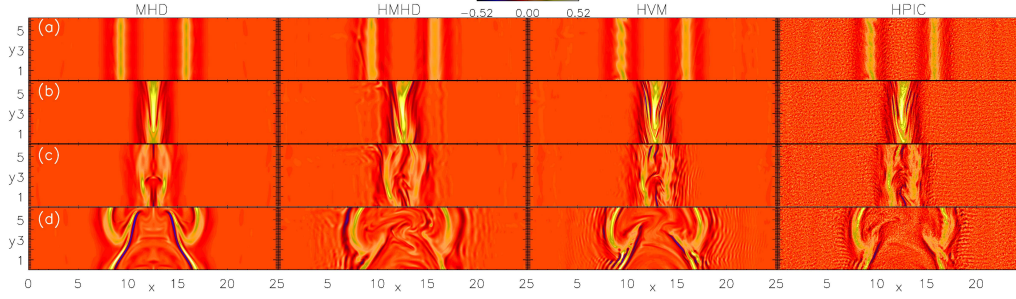


FIGURE 1. (Color online) Contour plot of the out of plane component of the current density $j_z(x, y)$ at several time instant $t = 29.5$ (a), $t = \tau = 58.9$ (b), $t = 70.7$ (c) and $t = 98.2$ (d). From left to right, each column refers to the MHD, HMHD, HVM and HPIC cases, respectively. For the HPIC simulation, $j_z(x, y)$ has been smoothed in order to remove particle noise.

Valentini *et al.* (2007). On the other hand, the hybrid PIC run has been performed using the P3D hybrid code (Zeiler *et al.* 2002) and all the numerical and physical parameters are the same as the HVM run. The code has been extensively used for reconnection and turbulence (e.g. Parashar *et al.* 2009; Malakit *et al.* 2009).

In both classes of performed simulation (fluid and kinetic), the spatial domain $D(x, y) = [0, 8\pi] \times [0, 2\pi]$ is discretized with $(N_x, N_y) = (1024, 256)$ in such a way that $\Delta x = \Delta y$ and spatial boundary conditions are periodic. For the HVM run, the velocity space is discretized with an uniform grid with 51 points in each direction, in the region $v_i = [-v_{max}, v_{max}]$ (being $v_{max} = 2.5\tilde{c}_A$) and velocity domain boundary conditions assume $f = 0$ for $|v_i| > v_{max}$ ($i = x, y, z$); while, in the HPIC case, the number of particles per cell is 400. Moreover $\beta_p = 2v_{th,p}^2/\tilde{c}_A^2 = \tilde{\beta}/2 = 0.5$ (i.e. $v_{max} = 5v_{th,p}$), $\mathbf{u}_e = \mathbf{u} - \tilde{\epsilon}\mathbf{j}/n$, $\tilde{\epsilon} = 9.8 \times 10^{-2}$, $k_{dp} = \tilde{\epsilon}^{-1} \simeq 10$ and $k_{de} = \sqrt{m_p/m_e} \times \tilde{\epsilon}^{-1} \simeq 100$. The background magnetic field is mainly perpendicular to the $x - y$ plane: $\mathbf{B}_0 = B_0(\sin \theta, 0, \cos \theta)$, where $\theta = \cos^{-1}[(\mathbf{B}_0 \cdot \hat{\mathbf{z}})/B_0] = 6^\circ$ and $B_0 = |\mathbf{B}_0|$.

In the initial conditions, ions are isotropic and homogeneous (Maxwellian velocity distribution function in each spatial point) for both kinetic simulations.

Large amplitude magnetic \mathbf{b} and bulk velocity \mathbf{u} perturbations are introduced, while no density perturbations are taken into account (which implies nonzero total pressure fluctuations). Initial perturbations consist of two Alfvénic wave packets with opposite velocity-magnetic field correlation. The packets are separated along x and, since $B_{0,x} \neq 0$, they counter-propagate. The nominal time for the collision, evaluated with respect to the center of each wave packet, is $\tau \simeq 58.9$.

The magnetic field perturbation \mathbf{b} has been built in such a way that $\mathbf{B}_0 \cdot \mathbf{b} = 0$ is satisfied in each spatial point. Then the velocity field perturbation \mathbf{u} is built by imposing that \mathbf{u} and \mathbf{b} are correlated (anti-correlated) for the wave packet which moves against (along) $B_{0,x}$. A detailed discussion about the properties of the initial perturbations can be found in Paper I. The condition $B = |\mathbf{B}| = \text{const}$ is not satisfied by our initial perturbations, while this condition would be a requirement in defining a large amplitude Alfvén mode in the context of a compressible MHD model. This suggests that pressure and density fluctuations are generated during the wave packet evolution.

The perturbations intensity is $\langle b \rangle_{rms}/B_0 = 0.2$, therefore the Mach number is $M_s = \langle u \rangle_{rms}/v_{th,p} = 0.4$. The intensity of fluctuations with respect to the in-plane field $B_{0,x}$ is quite strong, with a value of about 2. This last parameter can be associated with τ_{nl}/τ_{coll} (characteristic nonlinear time τ_{nl} ; characteristic collision time τ_{coll}), whose value gives

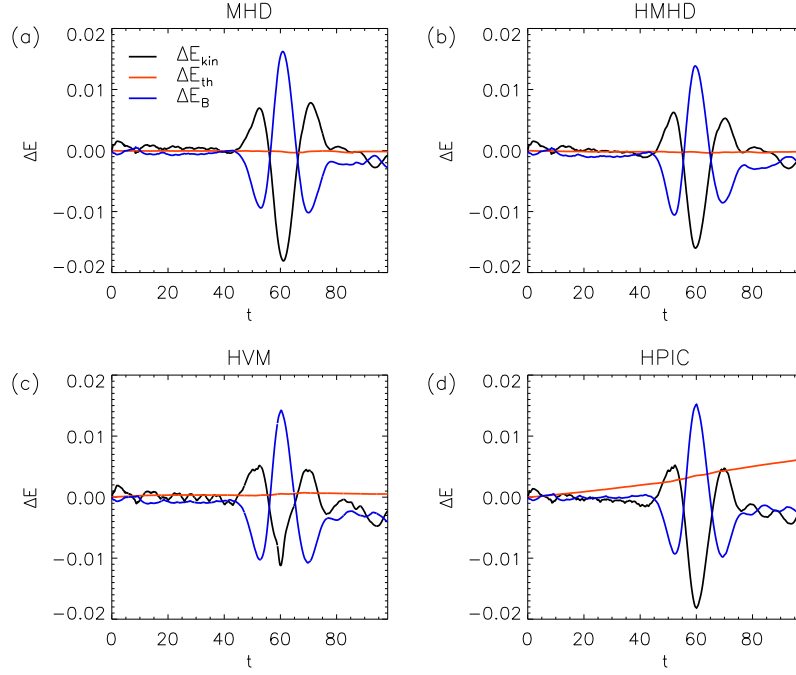


FIGURE 2. (Color online) Temporal evolution of the energy terms: ΔE_{kin} (black), ΔE_{th} (red) and ΔE_B (blue) for the MHD, HMHD, HVM and HPIC runs.

insight about the type of turbulence which could be generated. Here $\tau_{nl}/\tau_{coll} \simeq 0.5$, hence nonlinear effects are important to approach a strong turbulence scenario.

3. Numerical results: a comparison between several codes

In this Section we focus on the description of the results of the four different simulations (MHD, HMHD, HVM and HPIC) by focusing on some “fluid”-like diagnostics which help to understand the system dynamics and, also, to compare the numerical codes.

Figure 1 reports a direct comparison between the simulations, showing the contour plots of the out-of-plane component of the current density $j_z = (\nabla \times \mathbf{B}) \cdot \hat{\mathbf{z}}$. Vertical columns from left to right in Fig. 1 refer to MHD, HMHD, HVM and HPIC simulations, respectively; while each horizontal row refers to a different time instant: $t = 29.5$ (a), $t = \tau = 58.9$ (b), $t = 70.7$ (c) and $t = 98.2$ (d).

Significant differences are recovered in the MHD case with respect to the HMHD, HVM and HPIC runs. While the MHD evolution is symmetric with respect to the center of the x direction, in the other cases this symmetry is broken also before the wave packets interaction due to the presence of dispersive effects which differentiate the propagation along and across the background magnetic field. Moreover, during the wave packets overlap [Fig. 1(b)], smaller scales structures are formed in the HMHD and the HVM cases with respect to the pure MHD evolution, while the HPIC run - despite it recovers several significant features of the wave packets interaction - suffers the presence of particles thermal noise, which has been artificially smoothed out in Fig. 1.

After the collision [Fig. 1 (c) and (d)], the difference between the MHD and the other simulations becomes stronger. In particular, some vortical structures at the center of the spatial domain are recovered in the HMHD and HVM cases, in contrast to the pure

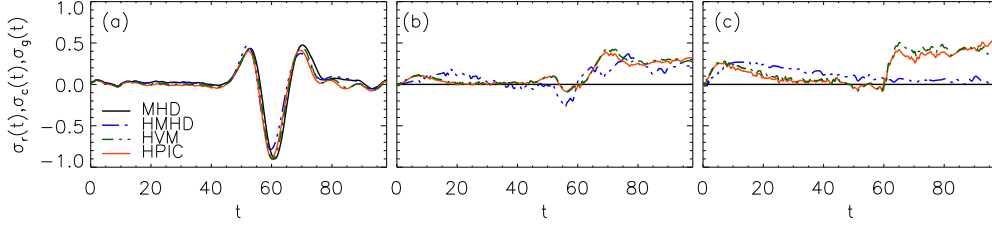


FIGURE 3. (Color online) Temporal evolution of the normalized residual energy $\sigma_r(t)$ (a), cross helicity $\sigma_c(t)$ (b) and generalized cross helicity $\sigma_g(t)$ (c). In each panel black, blue, green and red lines indicate the MHD, HMHD, HVM and HPIC simulations, respectively.

MHD case. Moreover, the Vlasov simulation exhibits some secondary ripples in front of each wave packet whose nature could be related to some wave-like fluctuations. These secondary, low-amplitude ripples are not recovered in the other simulations: in fact, they cannot be appreciated in the HPIC run where the noise prevents the formation of such structures while, in the Hall simulation, they are only roughly visible. The nature of these low-amplitude ripples is compatible with a KAW-like activity and will be reported in detail in a separate paper.

In order to compare models and codes, we display, in Fig. 2, the temporal evolution of the energy variations ΔE . Black, red and blue lines indicate respectively the kinetic ΔE_{kin} , thermal ΔE_{th} and magnetic ΔE_B energy variations, while each panel from (a) to (d) refers to the MHD, HMHD, HVM and HPIC runs, respectively. The evolution of ΔE_{kin} and ΔE_B is quite comparable in all the performed simulations and, in the temporal range where the wave packets collide, magnetic and kinetic energy is exchanged. On the other hand, the evolution of the thermal energy ΔE_{th} differs in the HPIC case compared to the other simulations. Indeed, ΔE_{th} remains quite close to zero for all the simulations except for the HPIC run, where it grows almost linearly for the presence of numerical noise. It is worth to note that, as the number of particles increases, the evolution of ΔE_{th} would get closer to the one obtained in the MHD, HMHD and HVM simulations.

The scenario described by Moffatt and Parker is also based on the property, in ideal incompressible MHD, that two wave packets separately conserve energy, which is equivalent to conservation of both total energy and cross helicity σ_c . It is natural therefore to examine evolution of cross helicity, as well as the evolution of the residual energy σ_r , which gives information about the relative strength of magnetic fluctuations and the fluid velocity fluctuations. Figures 3(a–b) show the temporal evolution of normalized residual energy σ_r (a) and the normalized cross-helicity σ_c (b). These quantities are defined as follows: $\sigma_r = (e^u - e^b)/(e^u + e^b) = 2e^r/(e^+ + e^-)$, where $e^r = e^u - e^b$, $e^\pm = \langle (\mathbf{z}^\pm)^2 \rangle / 2$ ($\mathbf{z}^\pm = \mathbf{u} \pm \mathbf{b}$), $e^u = \langle \mathbf{u}^2 \rangle / 2$ and $e^b = \langle \mathbf{b}^2 \rangle / 2$; $\sigma_c = (e^+ - e^-)/(e^+ + e^-) = 2e^c/(e^u + e^b)$, being $e^c = \langle \mathbf{u} \cdot \mathbf{b} \rangle / 2$. In each panel of Fig. 3, black, dashed blue, dashed green and red lines refer to MHD, HMHD, HVM and HPIC cases, respectively.

Figure 3 (a) shows the evolution of the normalized residual energy σ_r , which is similar in all the simulations. In particular $\sigma_r \simeq 0$ in the initial stage, it oscillates during the wave packets overlapping, and finally it returns to $\sigma_r \simeq 0$ after the collisions. The σ_r oscillations are well correlated with the oscillations of ΔE_B and ΔE_{kin} seen in Fig. 2.

Deeper insights are revealed by the evolution of the cross-helicity σ_c . Indeed, for ideal incompressible MHD, the cross helicity remains constant, and for this initial condition, $\sigma_c = 0$. Here, σ_c is well-preserved in the MHD run despite this simulation being compressible. This means that the compressible effects, introduced here by the fact that initial perturbations are not pressure balanced, are not strong enough to break the σ_c

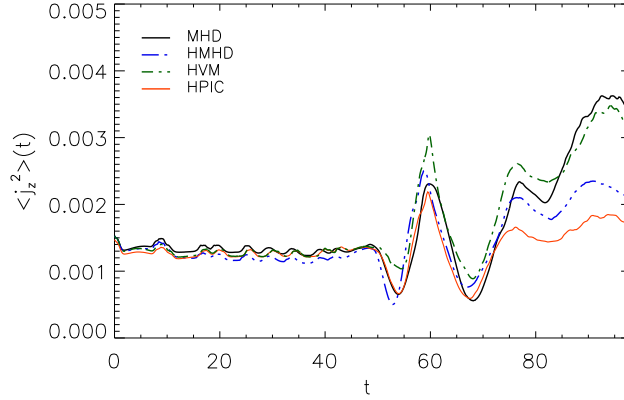


FIGURE 4. (Color online) Temporal evolution of $\langle j_z^2 \rangle$ for the MHD (black), HMHD (blue), HVM (green) and HPIC (red) simulations. For the HPIC simulation, $\langle j_z^2 \rangle$ has been smoothed in order to remove particle noise.

invariance. On the other hand, for the remaining simulations (HMHD, HVM and HPIC), σ_c is not preserved: i) it shows a jump around $t = \tau = 58.9$, due to the presence of kinetic and dispersive effects, and ii) there is an initial growth of σ_c followed by a relaxation phase. It seems also significant to point out that, the initial growth of σ_c occurs faster in the kinetic cases compared to the HMHD one. This may reflect the fact that, the initial condition evolves differently in the Hall MHD simulation compared to the kinetic runs.

In order to understand the role of the Hall physics, we computed the normalized generalized cross helicity $\sigma_g = 2e^g/(e^u + e^b)$, where $e^g = 0.5 \langle \mathbf{u} \cdot \mathbf{b} + \tilde{\epsilon} \omega \cdot \mathbf{u}/2 \rangle$, and $\omega = \nabla \times \mathbf{u}$, which is an invariant of incompressible HMHD (Turner 1986; Servidio *et al.* 2008). Figure 3(c) displays the temporal evolution of $\sigma_g(t)$ for the MHD (black), the HMHD (dashed blue), HVM (dashed green) and HPIC (red) simulations. Note that the evolution of σ_g is trivial for the MHD simulation where, since $\tilde{\epsilon} = 0$, $\sigma_g = \sigma_c$. Moreover, it can be easily appreciated that, for the HMHD case, σ_g is almost preserved and does not exhibit any significant variation due to the collision itself, even though it shows a slight increase in the initial stages of the simulation followed by a decay towards $\sigma_g = 0$ [similar to the growth of σ_c recovered in Fig. 3(b)]. On the other hand the two kinetic cases, which exhibit a similar behavior, show a fast growth of σ_g in the initial stage of the simulations followed by a decay phase [similar to the growth of σ_c recovered in Fig. 3(b)]; then, during the collision, σ_g significantly increases. We may explain the evolution of σ_c and σ_g as follows. In the MHD run, compressive effects contained in the initial condition as well as compressible activity generated during the evolution are not strong enough to break the invariance of σ_c (i.e. of σ_g). Instead, in the Hall MHD simulation, the first break of the σ_c invariance observed in the initial stage of the simulation cannot be associated with the Hall effect since also σ_g is not preserved in this temporal region and σ_c and σ_g have a similar evolution. On the other hand, the jump recovered in σ_c around $t \simeq \tau = 58.9$ is significantly related to the Hall physics. In fact, since σ_g does not exhibit a similar jump at $t \simeq \tau$, we argue that the physics which produces the growth of σ_c is the Hall physics (which is taken into account in the invariance of σ_g). Finally, the production of both σ_c and σ_g recovered in the kinetic simulations cannot be completely associated with the Hall effect (which, of course, is still present) but kinetic and compressive effects may have an important role.

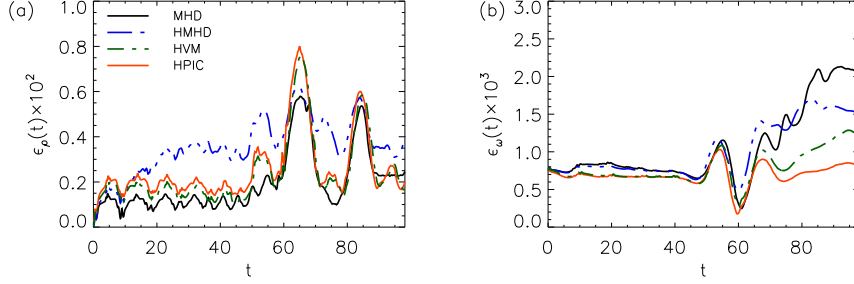


FIGURE 5. (Color online) Temporal evolution of $\epsilon_\rho(t)$ (a) and $\epsilon_\omega(t)$ (b). In each panel black, blue, green and red lines indicate the MHD, HMHD, HVM and HPIC simulations, respectively. For the HPIC simulation, $\epsilon_\omega(t)$ has been smoothed in order to remove particle noise.

In order to explore the role of small scales into the dynamics of colliding wave packets, we computed the averaged mean squared current density $\langle j_z^2 \rangle$ as a function of time. This quantity indicates the presence of small scale activity (such as production of small scale current sheets), and is reported in Figure 4 for all the simulations. As in the previous figures, black, blue dashed, green dashed and red lines refer to the MHD, HMHD, HVM and HPIC cases, respectively. All models show a peak of $\langle j_z^2 \rangle(t)$ around the collision time $t \simeq \tau$ due to the collision of wave packets. After the collision, some high-intensity current activity persists in all the simulations, which present a qualitatively similar evolution of $\langle j_z^2 \rangle(t)$.

Other quantities that provide physical details about our simulations are $\epsilon_\rho = \langle \delta \rho^2 \rangle$ (compressibility) and the enstrophy $\epsilon_\omega = \langle \omega^2 \rangle / 2$ (fluid vorticity ω). Note that $\delta \rho = \rho - \langle \rho \rangle$. Figure 5 reports the temporal evolution of ϵ_ρ (a) and ϵ_ω (b) for all the runs. Black, blue dashed, green dashed and red lines indicate respectively the MHD, HMHD, HVM and HPIC cases. The ϵ_ρ evolution shows that density fluctuations peak around $t \simeq 63.8$ and $t \simeq 83.4$. The two peaks are respectively associated with the collision between the packets and with the propagation of magneto-sonic fluctuations generated by the initial strong collision which provide a sort of “echo” of the original interaction. Moreover, from the initial stage of the simulations, ϵ_ρ exhibits some modulations, which are produced by the absence of a pressure balance in the initial condition. In fact, as packets start to evolve, low-amplitude fast perturbations (clearly visible in the density contour plots, not shown here) propagate across the box and collide faster compared to the “main” wave packets themselves. Moreover, by comparing the different simulations, one notices that, for $t \lesssim 20$, kinetic and Hall runs tend to produce a similar evolution of ϵ_ρ , slightly bigger compared to the MHD case. Then, around $t \simeq 20$, the HMHD run displays a stronger compressibility with respect to the kinetic cases. This difference is probably due to the presence of kinetic damping phenomena which occur in the kinetic cases.

The enstrophy ϵ_ω is displayed in Fig. 5(b). All the runs exhibit a similar evolution of ϵ_ω up to the wave packet collisions. Then MHD and HMHD cases exhibit a quite similar level of ϵ_ω , slightly bigger compared to the one recovered in the HVM and HPIC cases, where probably kinetic damping does not allow the formation of strong vortical structures at small scales.

It is interesting to compare different simulations also by looking at power spectral densities (PSDs). Figures 6 show the magnetic energy PSD integrated along k_y $E_{b,y}(k_x) = \sum_{k_y} E_b(k_x, k_y)$ (left column) and along k_x $E_{b,x}(k_y) = \sum_{k_x} E_b(k_x, k_y)$ (right column);

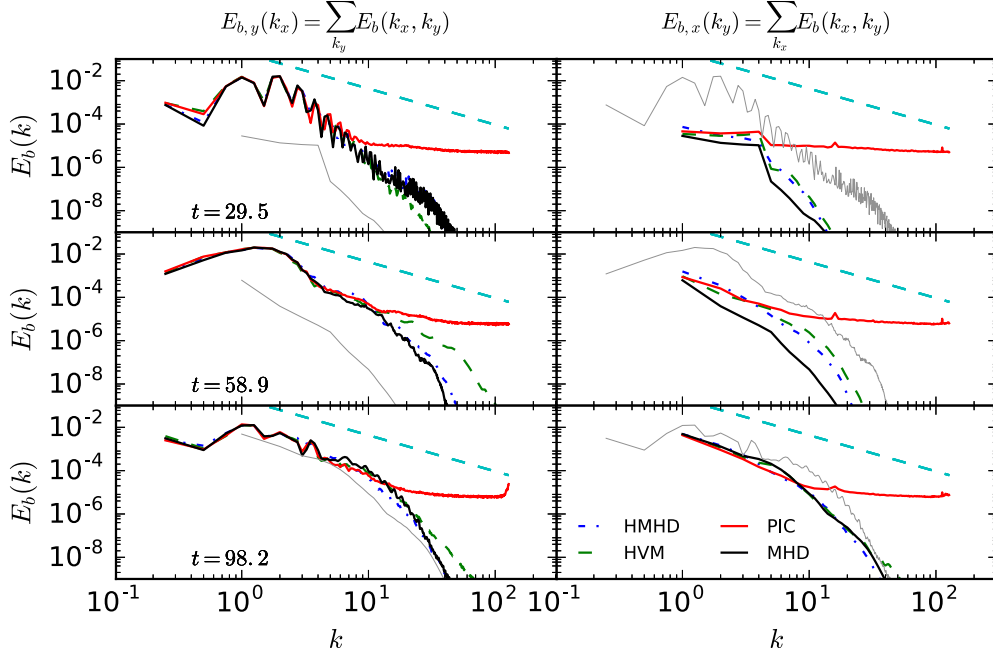


FIGURE 6. (Color online) Magnetic energy PSDs $E_{b,y}(k_x) = \sum_{k_y} E_b(k_x, k_y)$ (left column) and $E_{b,x}(k_y) = \sum_{k_x} E_b(k_x, k_y)$ (right column) at three time instants: $t = 29.5$ (top), $t = \tau = 58.9$ (middle) and $t = 98.2$ (bottom). In each panel black, blue, green and red lines refer to the MHD, HMHD, HVM and HPIC simulations, respectively; while cyan lines show the $-5/3$ slope for reference. Moreover, to compare $E_{b,y}(k_x)$ and $E_{b,x}(k_y)$, the gray lines in each panel refer only to the MHD simulation and report $E_{b,x}(k_y)$ in the left column and $E_{b,y}(k_x)$ in the right column.

while each row respectively refers to $t = 29.5$ (top row), $t = \tau = 58.9$ (center row) and $t = 98.2$ (bottom row). The cyan dashed line shows the $k^{-5/3}$ slope for reference while, in each panel, black, blue, dashed green and red lines indicate respectively MHD, HMHD, HVM and HPIC simulations. Moreover, to compare the two wave-number directions, gray lines in each panel report the corresponding PSD obtained from the MHD run, reduced in the other direction [for example, in the top row left panel, the gray line refers to $E_{b,x}(k_y)$ for the MHD simulation while other curves in the same panel report $E_{b,y}(k_x)$]. It is interesting to note that, at $t = 29.5$, all the simulations exhibit a steep spectrum in $E_{b,y}(k_x)$, related to the initial condition, while the difference in power between $E_{b,y}(k_x)$ and $E_{b,x}(k_y)$ - the latter being significantly smaller than the former - tends to reduce in the final stages of the simulations. This suggests, as described in Paper I, the presence of nonlinear couplings which cause spectra to become more isotropic. Moreover the comparison between the different simulations indicates that the dynamics at large scales is described in a quite similar way by all runs, while at small scales some differences are revealed. In particular, the HPIC simulation is affected by particles noise while the HVM run contains more energy at small scales compared to MHD and HMHD. Note that the presence, in MHD and HMHD runs, of an explicit resistivity prevents the population of small scales.

To summarize this section, we compared our numerical codes by analyzing some global diagnostics and we conclude that the Moffatt-Parker scenario is quite well satisfied by MHD. However, other intriguing characteristics are observed when one moves beyond the

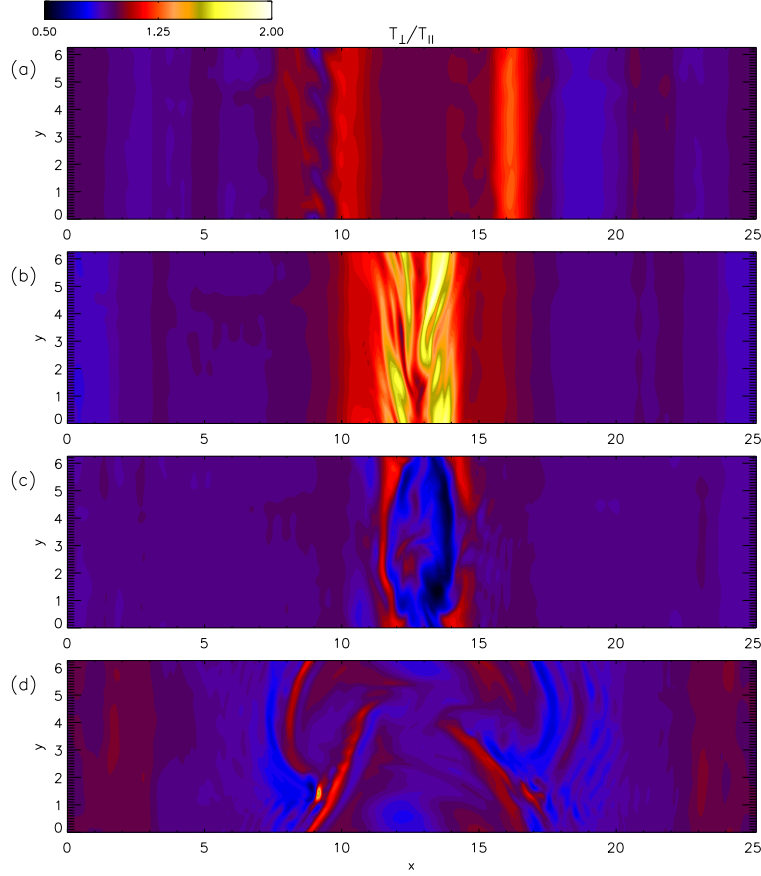


FIGURE 7. (Color online) Contour plots of the temperature anisotropy, for the HVM run, evaluated in the LBF at four time instants: (a) $t = 29.5$, (b) $t = \tau = 58.9$, (c) $t = 70.7$ and (d) $t = 98.2$.

MHD treatment. Moreover, the comparison between kinetic codes suggests that HVM and HPIC simulations display qualitatively similar features at large scales. However, when one aims to analyze the dynamics at small scales, HPIC simulations suffers from thermal particle noise. Magnetic energy spectra differ in the HPIC case compared with the HVM case. Moreover, by comparing the j_z contour plots, one can easily appreciate how HPIC simulation is affected by particle noise. Based on these considerations, we continue the analysis of the kinetic features produced in Alfvén wave packet collisions by focusing only on the HVM case.

4. Kinetic features recovered during the wave packets interaction

We begin a description of the kinetic signatures present in the Vlasov simulation by looking at the temperature anisotropy. Fig. 7 reports the contour plots of the temperature anisotropy T_{\perp}/T_{\parallel} , where the parallel and perpendicular directions are evaluated in the local magnetic field frame (LBF), at four time instants: $t = 29.5$ (a), $t = \tau = 58.9$ (b), $t = 70.7$ (c) and $t = 98.2$ (d). Clearly temperature anisotropy is present even before the main wave packets collision, due to the fact that the initial wave packets are not

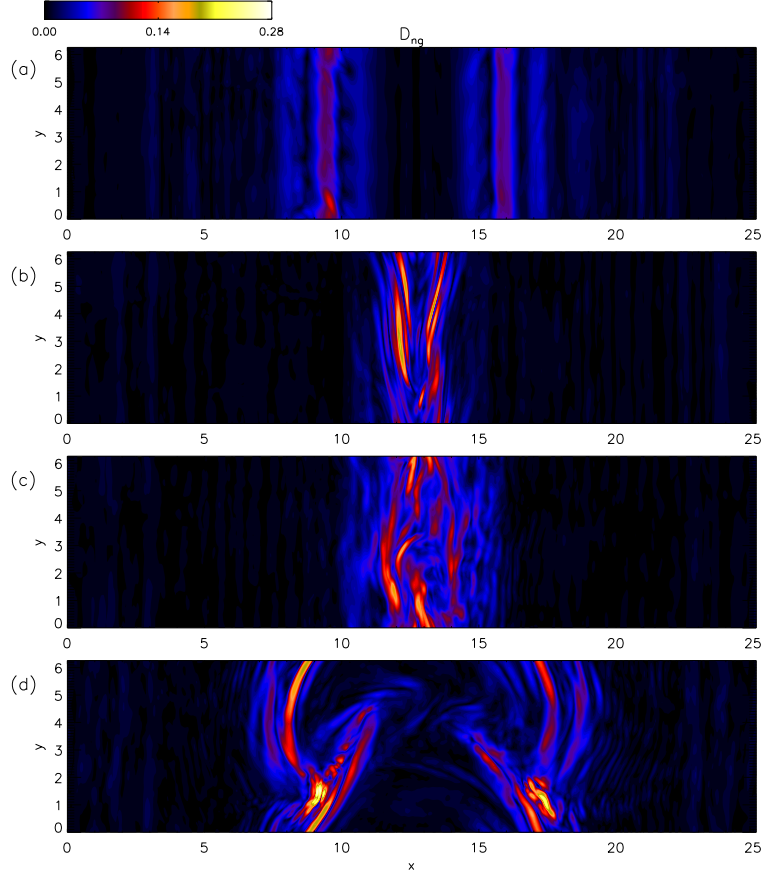


FIGURE 8. (Color online) Contour plots of the degree of temperature non-gyrotropy D_{ng} , for the HVM run, evaluated in the LBF at four time instants: (a) $t = 29.5$, (b) $t = \tau = 58.9$, (c) $t = 70.7$ and (d) $t = 98.2$.

linear eigenmodes of the Vlasov equation and, hence, their dynamical evolution leads to an anisotropy production. Moreover, a more careful analysis suggests that the left wave packet tends to produce regions where $T_{\perp}/T_{\parallel} < 1$ close to the packet itself (which, as it can be appreciated in Fig. 1, is localized around $x \simeq 9.5$), while the right wave packet (localized around $x = 15.7$) is characterized by $T_{\perp}/T_{\parallel} > 1$. The presence of different temperature anisotropies is related to the broken symmetry with respect to the center of the x direction. Indeed, the dynamics of the wave packets is different if they move parallel or anti-parallel to $B_{0,x}$. This produces the different temperature anisotropy recovered in the top panel of Fig. 7.

When the packets collide [Fig. 7 (b)], sheets characterized by a strong temperature anisotropy ($T_{\perp}/T_{\parallel} > 1$) are recovered, correlated spatially with the current density structures. Then, at $t = 70.7$ [Fig. 7 (c)], wave packets split again and a region, localized at $(x, y) \simeq (14.3, 1.0)$, where the temperature anisotropy suddenly moves from values $T_{\perp}/T_{\parallel} < 1$ towards $T_{\perp}/T_{\parallel} > 1$ ones is present. We will show that this region also shows the presence of strong departures from the equilibrium Maxwellian shape. At the final stage of the simulations [Fig. 7 (d)], each wave packet continues traveling, accom-

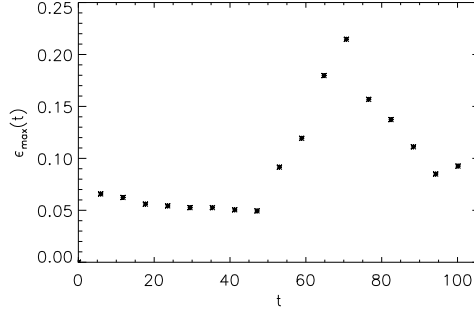


FIGURE 9. (Color online) Temporal evolution of $\epsilon_{max}(t)$ for the HVM run.

panied by a persistent level of temperature anisotropy, which is, indeed, well correlated with the current structures.

It is interesting to point out that, beyond the presence of temperature anisotropies, regions characterized by a temperature nongyrotropy are also recovered. Many methods have been proposed by evaluating the temperature nongyrotropy (Aunai *et al.* 2013; Swisdak 2016). Here we adopt the measure D_{ng} (Aunai *et al.* 2013), which is proportional to the root-mean-square of the off-diagonal elements of the pressure tensor. Fig. 8 shows the contour plots of D_{ng} at four time instants: $t = 29.5$ (a), $t = \tau = 58.9$ (b), $t = 70.7$ (c) and $t = 98.2$ (d). Moreover, as for the temperature anisotropy, the evolution of the two wave packets tends to produce temperature nongyrotropies also before the wave packets collision [Fig. 8(a)]. Then, during the collision [Fig. 8(b)–(c)], the temperature nongyrotropy becomes more intense and it is also quite well correlated with the current structures. At the final stage of the simulation [Fig. 8(d)], each wave packet is connoted by a level of nongyrotropy which is quite bigger compared to the value before the collision. The presence of nongyrotropic regions suggests that it is fundamental to retain a full velocity space where the VDF is let free to evolve and, eventually, distort.

To further support the idea that kinetic effects are produced during the interaction of the wave packets, we computed the L^2 norm difference (Servidio *et al.* 2012; Greco *et al.* 2012; Servidio *et al.* 2015):

$$\epsilon(x, y, t) = \frac{1}{n} \sqrt{\int [f(\mathbf{x}, \mathbf{v}, t) - f_M(\mathbf{x}, \mathbf{v}, t)]^2 d\mathbf{v}} \quad (4.1)$$

which measures the displacements of the proton VDF $f(\mathbf{x}, \mathbf{v}, t)$ with respect to the associated Maxwellian distribution function $f_M(\mathbf{x}, \mathbf{v}, t)$, built such that density, bulk speed and total temperature of the two VDFs are the same. Figure 9 reports the evolution of the $\epsilon_{max}(t) = \max_{(x,y)} \epsilon(x, y, t)$ as a function of time. Clearly, as for the previous proxies of kinetic effects, also ϵ_{max} moves away from zero in the early phases of the simulation due to the fact that the initial-condition is not a Vlasov eigenmode. Moreover, after the first initial variation, ϵ_{max} is almost constant until wave packets interact. Then, during the collision, ϵ_{max} grows and reaches its maximum at $t = 70.7$, quite later than the wave packet collisions. Then it decreases and saturates at a value about two times bigger than the value before the collision, thus suggesting, again, that there is “net” production of non-Maxwellian features in the VDF during the wave packets interaction.

In order to appreciate the structure of ϵ in the spatial domain, the left panel of Figure 10 shows the contour plot of $\epsilon(x, y, t)$ at the time instant $t = 70.7$ (when ϵ reaches its maximum value). The ϵ contours are correlated with the current structures and with

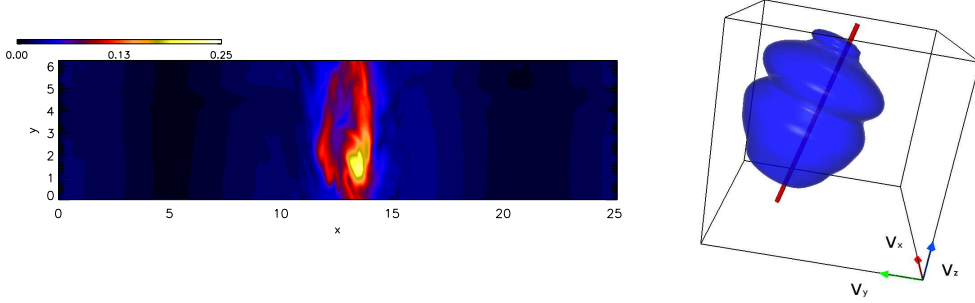


FIGURE 10. (Color online) (Left) Contour plots of $\epsilon(t)$, for the HVM run, at $t = 70.7$. (Right) Proton distribution functions, in the spatial point (x^*, y^*) where $\epsilon(x^*, y^*, t) = \max_{(x,y)} \epsilon(x, y, t)$ at $t = 70.7$. The local magnetic field direction is indicated by a red line.

the anisotropic/nongyrotropic regions. Moreover, a blob-like region where ϵ reaches its maximum is present. This area is associated with the region where the temperature anisotropy moves from $T_{\perp}/T_{\parallel} < 1$ values towards $T_{\perp}/T_{\parallel} > 1$ ones [See Fig. 7(c)]. In this area the VDF strongly departs from the Maxwellian. The right panel of Fig. 10 shows the three dimensional isosurface plot of the VDF at $t = 70.7$ and in the spatial point (x^*, y^*) where $\epsilon(x^*, y^*, t = 70.7) = \max_{(x,y)} \epsilon(x, y, t = 70.7)$. A strong beam, parallel to the local magnetic field direction, is observed in the VDF in Fig. 10. The drift speed of the beam is about \tilde{c}_A . The production of a beam due to the interaction of two wave packets has been also pointed out by He *et al.* (2015).

5. Conclusion

In this paper we have described the interaction of two Alfvénic wave packets by means of MHD, Hall MHD and hybrid kinetic simulations of the same physical configuration. Kinetic simulations have been performed with two different codes: an Eulerian Vlasov-Maxwell code (Valentini *et al.* 2007) and hybrid Particle-in-cell code (Parashar *et al.* 2009). By approaching the *Parker & Moffatt* problem within several physical frameworks, we have comparatively analyzed different effects (compressive, Hall and kinetic) which contribute to the general, complex puzzle.

The analysis performed in Paper I where MHD and Vlasov simulations were compared has been here extended by including the Hall MHD framework. In particular, we showed how, moving beyond the pure MHD treatment, dispersion as well as kinetic effects play an important role. Furthermore, the analysis of HMHD and kinetic runs allows to separate the presence of dispersive and purely kinetic features. It is also interesting to note that the compressive activity is different in the Hall case compared to the kinetic runs, indicating that some kinetic damping processes may be active in the Vlasov simulation. A separate type of comparison is afforded by comparative analysis of the HPIC and HVM runs, While these methods should describe, approximately, the same physics, i.e., the Vlasov treatment of collisionless plasma dynamics, the comparison between the different codes is interesting from a methodological perspective, and therefore represents a contribution to the Turbulent Dissipation Challenge (Parashar *et al.* 2015b). In particular, the two kinetic simulations performed are able to take into account the dynamics which occurs at large spatial scales and their comparison is successful in this range of scales. However the PIC runs lacks accuracy when smaller spatial scales are produced by the collision of the two wave packets, thus indicating that the Eulerian approach better describes the

dynamics of the system at small spatial scales. Of course the comparison is expected to become better if the number of particle per cell in the PIC simulation gets bigger (Camporeale & Burgess 2011; Franci *et al.* 2015(@).

Based on the last consideration, we have analyzed the production of kinetic signatures by focusing only on the HVM simulation. Several proxies which are routinely adopted for highlighting the presence of kinetic features indicate that wave packets tend to produce kinetic effects such as temperature anisotropies and nongyrotropies also before the main wave packets interaction. This is related to the fact that the initial condition, consisting of quasi-Alfvénic wave packets, is neither a Vlasov equilibrium nor a Vlasov eigenmode. Therefore it dynamically leads to the production of kinetic features.

The analysis of kinetic effects before and after the main wave packets collision indicates that some kinetic features are enhanced by the collision itself and each wave packet is significantly characterized by a strong degree of non-thermal signatures. In particular the presence of temperature nongyrotropies suggests that descriptions based on reduced velocity space assumptions may partially fail the description of such features. Finally, similarly to the observations of He *et al.* (2015), during the wave packet collision, a beam in the velocity distribution function is observed to form along the direction of the local magnetic field. This characteristic may connect our results with the general scenario of wave packets observed in natural plasmas such as the solar wind.

Research is supported by NSF AGS-1063439, AGS-1156094 (SHINE), AGS-1460130 (SHINE), and NASA grants NNX14AI63G (Heliophysics Grandchallenge Theory), and the Solar Probe Plus science team (ISIS/SWRI subcontract No. D99031L), and Agenzia Spaziale Italiana under the contract ASI-INAF 2015-039-R.O Missione M4 di ESA: Partecipazione Italiana alla fase di assessment della missione THOR. Kinetic numerical simulations here discussed have been run on the Fermi supercomputer at Cineca (Bologna, Italy), within the ISCRA-C project IsC37-COLALFWP (HP10CWCE72) and on the Newton parallel machine at University of Calabria (Rende, Italy).

REFERENCES

- ALEXANDROVA, O., CARBONE, V., VELTRI, P. & SORRISO-VALVO, L. 2008 Small-scale energy cascade of the solar wind turbulence. *The Astrophysical Journal* **674**, 1153.
- AUNAI, N., HESSE, M. & KUZNETSOVA, M. 2013 Electron nongyrotropy in the context of collisionless magnetic reconnection. *Physics of Plasmas* **20**, 092903.
- BARNES, A. 1979 *Space Plasma Physics: The Study of Solar-System Plasmas* (National Academy of Sciences, Washington, DC USA).
- BELCHER, J.W., & DAVIS JR., L. 1971 Largeamplitude Alfvén waves in the interplanetary medium, 2. *J. Geophys. Res.* **76**, 3534.
- BIRDSALL, C.K., & LANGDON, A.B. 2004 *Plasma physics via computer simulation* (CRC Press).
- BRUNO, R., BAVASSANO, R., & VILLANTE, U. 1985 Evidence for long period Alfvén waves in the inner solar system. *J. Geophys. Res.* **90**, 4373.
- BRUNO, R. & CARBONE, V. 2013 The solar wind as a turbulence laboratory. *Living Reviews in Solar Physics* **10**, 1–208.
- CAMPOREALE, E. & BURGESS, D. 2011 The dissipation of solar wind turbulent fluctuations at electron scales. *The Astrophysical Journal* **730**, 114.
- DAWSON, J.M. 1932 Particle simulation of plasmas. *Reviews of Modern Physics* **55**, 403.
- DOBROWOLNY, M., MANGENEY, A. & VELTRI, P. 1980 Fully developed anisotropic hydromagnetic turbulence in interplanetary space. *Phys. Rev. Lett.* **45**, 144.
- DOBROWOLNY, M., MANGENEY, A. & VELTRI, P. 1980 Properties of magnetohydrodynamic turbulence in the solar wind. *Solar and Interplanetary Dynamics* (Springer, Netherlands).
- ELSÄSSER, W.M. 1950 The hydromagnetic equations. *Phys. Rev.* **79**, 183.
- FRANCI, L., VERDINI, A., MATTEINI, L., LANDI, S. & HELLINGER, P. 2015 Solar wind turbu-

- lence from MHD to sub-ion scales: high resolution hybrid simulations. *The Astrophysical Journal Letters* **804**, L39.
- GALTIER, S., NAZARENKO, S.V., NEWELL, A.C. & POUCKET, A. 2000 A weak turbulence theory for incompressible magnetohydrodynamics. *J. Plasma Physics* **63**, 447.
- GARY, S.P., SAITO, S. & NARITA, Y. 2010 Whistler turbulence wavevector anisotropies: Particle-in-cell simulations. *The Astrophysical Journal* **716**, 1332.
- GOLDREICH, P., & SRIDHAR, S. 1995 Toward a theory of interstellar turbulence. 2: Strong Alfvénic turbulence. *The Astrophysical Journal* **438**, 763.
- GRECO, A., VALENTINI, F., SERVIDIO, S. & MATTHAEUS, W.H. 2012 Inhomogeneous kinetic effects related to intermittent magnetic discontinuities. *Physics Review E* **86**, 066405.
- HE, J., TU, C., MARSCH, E., CHEN, C.H.K., WANG, L., PEI, Z., ZHANG, L., SALEM C.S. & BALE, S.D. 2015 Proton heating in solar wind compressible turbulence with collisions between counter-propagating waves. *The Astrophysical Journal Letters* **83**, L30.
- HOWES, G.G. & NIELSON, K.D. 2013 Alfvén wave collisions, the fundamental building block of plasma turbulence. I. Asymptotic solution. *Phys. Plasmas* **20**, 072302.
- HOWES, G.G. 2015 The inherently three-dimensional nature of magnetized plasma turbulence. *Journal of Plasma Physics* **81**, 325810203.
- IROSHNIKOV, R.S. 1964 Turbulence of a conducting fluid in a strong magnetic field. *Soviet Astron.* **7**, 566.
- LION, S., ALEXANDROVA, O., & ZASLAVSKY, A. 2016 Coherent events and spectral shape at ion kinetic scales in the fast solar wind turbulence. *The Astrophysical Journal* **824**, 47.
- KARIMABADI, H., ROYTERSHTEYN, V., DAUGHTON, W., & LIU Y. 2013 Recent Evolution in the Theory of Magnetic Reconnection and Its Connection with Turbulence. *Space Science Reviews* **178**, 307.
- KRAICHNAN, R.H. 1965 Inertialrange spectrum of hydromagnetic turbulence. *Phys. Fluids* **8**, 1385–1387.
- LI, T.C., HOWES, G.G., KLEIN, K.G., & TENBARGE, J.M. 2016. Energy dissipation and Landau damping in two- and three-dimensional plasma turbulence. *The Astrophysical Journal Letters* **832**, L24.
- MALAKIT, K., CASSAK, P.A., SHAY, M.A. & DRAKE, J.F. 2009 The Hall effect in magnetic reconnection: Hybrid vs. Hall-less hybrid simulations. *Geophysical Research Letters* **36**, L07107.
- MARSCH, E. 2006 Kinetic physics of the solar corona and solar wind. *Living Rev. Sol. Phys.* **3**, 1–100.
- MATTHAEUS, W.H., ZANK, G.P., SMITH, C.W., & OUGHTON, S. 1999 Turbulence, Spatial Transport, and Heating of the Solar Wind. *Phys. Rev. Lett.* **82**, 3444.
- MATTHAEUS, W.H., ZANK, G.P., OUGHTON, S., MULLAN, D.J. & DMITRUK, P. 1999 Coronal heating by magnetohydrodynamic turbulence driven by reflected low-frequency waves, *The Astrophysical Journal Letters* **523**, L93.
- MOFFATT, H.K. 1978 *Field Generation in Electrically Conducting Fluids* (Cambridge University Press)
- NG, C.S., & BHATTACHARJEE, A. 1996 Interaction of shear-Alfvén wave packets: implication for weak magnetohydrodynamic turbulence in astrophysical plasmas. *The Astrophysical Journal* **465**, 845.
- NIELSON, K.D., HOWES, G.G. & DORLAND, W. 2013 Alfvén wave collisions, the fundamental building block of plasma turbulence. II. Numerical solution. *Phys. Plasmas* **20**, 072303.
- PARASHAR, T.N., SHAY, M.A., CASSAK, P.A. & MATTHAEUS, W.H. 2009 Kinetic dissipation and anisotropic heating in a turbulent collisionless plasma. *Physics of Plasmas* **16**, 032310.
- PARASHAR, T.N., MATTHAEUS W.H., SHAY, M.A., & WAN, M. 2015 (a) Transition from Kinetic to MHD Behavior in a Collisionless Plasma. *The Astrophysical Journal* **811**, 112.
- PARASHAR, T.N., SALEM, C., WICKS, R.T., KARIMABADI, H., GARY, S.P., & MATTHAEUS, W.H. 2015 (b) Turbulent dissipation challenge: a community-driven effort. *J. Plasma Phys.* **81**, 905810513.
- PARASHAR, T.N., OUGHTON, S., MATTHAEUS W.H., & WAN, M. 2016 Variance anisotropy in kinetic plasmas. *The Astrophysical Journal* **824**, 44.
- PARKER, E.N. 1979 *Cosmical magnetic fields: Their origin and their activity* (Oxford University Press)

- PERRONE, D., ALEXANDROVA, O., MANGENEY, A., MAKSIMOVIC, M., LACOMBE, C., RAKOTO, V., KASPER, J.C., & JOVANOVIĆ, D. 2016 Compressive coherent structures at ion scales in the slow solar wind. *The Astrophysical Journal* **826**, 196.
- PEZZI, O., PARASHAR, T.N., SERVIDIO, S., VALENTINI, F., VÁSCONEZ, C.L., YANG, Y., MALARA, F., MATTHAEUS, W.H. & VELTRI, P. 2016 Revisiting a classic: the Parker-Moffatt problem *The Astrophysical Journal* **834**, 166.
- PUCCI, F., VÁSCONEZ, C.L., PEZZI, O., SERVIDIO, S., VALENTINI, F., MATTHAEUS, W.H. & MALARA, F. 2016 From Alfvén waves to kinetic Alfvén waves in an inhomogeneous equilibrium structure. *Journal of Geophysical Research* **121**, 1024–1045.
- ROBERTS, O.W., LI, X., ALEXANDROVA, O., & LI, B. 2016 Observations of an MHD Alfvén vortex in the slow solar wind. *J. Geophys. Res.* **121**, 3870.
- SAHRAOUI, F., GALTIER, S., & BELMONT, G. 2007 On waves in incompressible Hall magneto-hydrodynamics. *J. Plasma Phys.* **73**, 723.
- SERVIDIO, S., MATTHAEUS, W.H. & CARBONE, V. 2008 Statistical properties of ideal three-dimensional Hall magnetohydrodynamics: The spectral structure of the equilibrium ensemble. *Phys. Plasmas*, **15**, 042314.
- SERVIDIO, S., VALENTINI, F., CALIFANO, F. & VELTRI, P. 2012 Local kinetic effects in two-dimensional plasma turbulence. *Phys. Rev. Lett.* **108**, 045001.
- SERVIDIO, S., VALENTINI, F., PERRONE, D., GRECO, A., CALIFANO, F., MATTHAEUS W.H., & VELTRI, P. 2015 A kinetic model of plasma turbulence. *Journal of Plasma Physics* **81**, 328510107.
- SRIDHAR, S., & GOLDBREICH, P. 1994 Toward a theory of interstellar turbulence. 1: Weak Alfvénic turbulence. *The Astrophysical Journal* **432**, 612.
- SWISDAK, M. 2016 Quantifying gyrotropy in magnetic reconnection. *Geophysical Research Letters* **43**, 43–49.
- TOMCZYK, S., MCINTOSH, S. W., KEIL, S. L., JUDGE, P. G., SCHAD, T., SEELEY, D. H., & EDMONDSON, J. 2007 Alfvén waves in the solar corona. *Science* **317**, 1192.
- TURNER, L. 1986 Hall effects of magnetic relaxation. *IEEE Transactions on Plasma Science* **14**, 849–857.
- VALENTINI, F., TRAVNICEK, P., CALIFANO, F., HELLINGER, P. & MANGENEY, A. 2007 A hybrid-Vlasov model based on the current advance method for the simulation of collisionless magnetized plasma. *Journal of Computational Physics* **225**, 753.
- VALENTINI, F., CALIFANO, F., PERRONE, D., PEGORARO, F., & VELTRI, P. 2011 New ion-wave path in the energy cascade. *Physical review letters* **106**, 165002.
- VALENTINI F., SERVIDIO S., PERRONE D., CALIFANO F., MATTHAEUS W. H. & VELTRI, P. 2014 Hybrid Vlasov-Maxwell simulations of two-dimensional turbulence in plasmas. *Physics of Plasmas* **21**, 082307.
- VÁSCONEZ, C.L., PUCCI, F., VALENTINI, F., SERVIDIO, S., MATTHAEUS, W.H. & MALARA, F. 2015 Kinetic Alfvén wave generation by large-scale phase mixing. *The Astrophysical Journal* **815**, 7.
- VELLI, M., GRAPPIN, R. & MANGENEY, A. 1989 Turbulent cascade of incompressible unidirectional Alfvén waves in the interplanetary medium. *Phys. Rev. Lett.* **63**, 1807.
- VERDINI, A., VELLI, M., & BUCHLIN, E. 2009 Turbulence in the sub-Alfvénic solar wind driven by reflection of low-frequency Alfvén waves. *The Astrophys. Journal Letters* **700**, L39.
- WAN, M., MATTHAEUS, W.H., ROYTERTSHTYEN, V., KARIMABADI, H., PARASHAR, T., WU, P., & SHAY, M. 2015 Intermittent Dissipation and Heating in 3D Kinetic Plasma Turbulence. *Phys. Rev. Lett.* **114**, 175002 (2015).
- ZEILER, A., BISKAMP, D., DRAKE, J.F., ROGERS, B.N., SHAY, M.A. & SCHOLER, M. (2002) Three-dimensional particle simulations of collisionless magnetic reconnection. *J. Geophys. Res.* **107**, 1230.